Title

Evaluation of a Large Area, 83 μm Pixel Pitch Amorphous Selenium Indirect Flat Panel Detector.

Journal

IEEE Transactions on Electron Devices, 71(1)

ISSN

0018-9383

Authors

Hellier, Kaitlin
Mollov, Ivan
Swaby, Akyl
et al.

Publication Date

2024

DOI

10.1109/ted.2023.3338131

Published in final edited form as:
IEEE Trans Electron Devices. 2024 January ; 71(1): 676–680. doi:10.1109/ted.2023.3338131.

Evaluation of a Large Area, 83 μm Pixel Pitch Amorphous Selenium Indirect Flat Panel Detector

Kaitlin Hellier [Member, IEEE],
Electrical and Computer Engineering Department, University of California at Santa Cruz, Santa Cruz, CA 95064 USA

Ivan Mollov,
Varex Imaging Corporation, Santa Clara, CA 95134 USA.

Akyl Swaby [Graduate Student Member, IEEE],
Electrical and Computer Engineering Department, University of California at Santa Cruz, Santa Cruz, CA 95064 USA

Paul Pryor,
Varex Imaging Corporation, Santa Clara, CA 95134 USA.

Shiva Abbaszadeh [Senior Member, IEEE]
Electrical and Computer Engineering Department, University of California at Santa Cruz, Santa Cruz, CA 95064 USA

Abstract

Dual-layer detectors provide a low-cost solution to improved material decomposition and lesion differentiation in X-ray imaging, while eliminating motion artifacts from multiple exposures. Most designs utilize two indirect detectors with scintillators designed for low-energy and higher-energy detection and separated by a copper filter to harden the beam for high energy detection. To improve the performance of the bottom detector and lower dose requirements, we have previously proposed an alloyed amorphous selenium photodetector to achieve improved resolution and absorption at green wavelengths, better suited to high-performance scintillators such as CsI:Tl. In this work, we demonstrate a baseline prototype for the bottom layer—a continuous, large area 83 μm pixel pitch flat panel indirect detector with well-established amorphous selenium as the photodetector—and verify the architecture's performance and detector design. We characterize lag, noise-power spectrum, detective quantum efficiency, and modular transfer function of the detector, and show resolution up to 6 lp/mm when operated at an applied bias of 150 V. This provides a starting point for evaluating the alloyed selenium materials, and shows promise for this detector in the future dual-layer design.

Corresponding author: khellier@ucsc.edu.

Keywords

Amorphous selenium; flat panel detector (FPD); indirect detector; large area detector; X-ray detector

I. Introduction

Recent years have seen significant development in X-ray imaging detector technology, ranging from improvements in resolution to energy-discriminating photon counting. [1], [2], [3], [4], [5], [6], [7] thin-film transistor (TFT) flat panel detectors (FPDs) are the most common commercially employed detectors, though average the absorbed X-ray spectrum and do not have energy resolution capabilities. This limits their ability to differentiate lesions from dense tissue and provide material decomposition. To accurately identify material densities, resolving the energy of the received X-ray quanta is necessary [8], [9].

Energy differentiation can be achieved by three main techniques: photon counting, dual-shot detection, and dual-layer detectors. Each has its drawbacks, whether cost, motion artifacts, or dosage [10], [11], [12], [13], [14], [15]. Dual-layer detection uses a single, polyenergetic X-ray exposure to resolve low and high energies by using two stacked detectors. The single exposure avoids motion artifacts and improves detectability, however, requires a higher dose than photon counting detectors. The lower energy X-rays are absorbed by the first detector, then the remaining, higher energy X-rays are usually hardened to increase energy differentiation by a copper filter before being absorbed by the next higher energy detector. This beam hardening photon starves the second layer, which requires increasing X-ray intensity and dose to the patient to achieve an acceptable signal in the detector [16], [17], [18], [19].

In order to reduce the dose to the patient while achieving dual-energy, high-resolution images, we’ve proposed a direct/indirect dual-layer architecture [20], [21]. The bottom layer will employ an indirect FPD with an alloyed a-Se photodetector high for higher energies. Amorphous selenium is a high absorption and resolution semiconductor, capable of uniform large-area, low-cost fabrication [22], [23], [24], [25]. It has been well studied and is already in use in commercial mammography detectors [26], [27]. The capability of impact ionization in a-Se has been utilized in high-gain avalanche rushing amorphous photoconductor (HARP) detectors, allowing for gains greater than unity at fields less than 80 V/μm [28]. Scheuermann et al. [29] have demonstrated its capability as a large area indirect conversion FPD, showing high resolution, DQE, and modulation transfer function (MTF).

Ideally, a CsI:Tl scintillator will be paired with the photodetector, utilizing its high photon yield from X-ray absorption and improved resolution over other scintillators. However, the emission energy of CsI:Tl falls below a-Se’s mobility gap energy, limiting its effectiveness. Previous studies from this group demonstrate the tunability of a-Se by alloying with tellurium (Te), in which the band gap can be reduced while achieving high conversion efficiency for thick Se-Te devices [30]. These detectors show increased performance at longer wavelengths, enhancing performance in the region of CsI:Tl emission. This, combined with the ability to achieve impact ionization at low fields, makes Se-Te ideal for the photoconductor in the indirect layer, as a lower dose can be used while generating an acceptable signal [31], [32], [33].

In order to evaluate the proposed detector performance, we must first set a baseline to compare to. Following work that studies a single pixel device to test the performance of parylene blocking layers [21], we present preliminary studies on an indirect a-Se FPD bottom layer, verifying the viability of the chosen photodetector architecture with well-established a-Se. We demonstrate the performance of the continuous large area (85 × 85 mm), 83 μm pixel pitch FPD paired with common scintillators, in preparation for the fabrication of an alloyed FPD capable of impact ionization.

II. Methods

A. Fabrication

The 85 × 85 mm active area FPD was constructed by depositing several layers of material on a Varex TFT backplane with an 83 μm pixel pitch; the architecture can be seen in a cross-sectional schematic in Fig. 1. First, a 100 nm planarization layer of parylene-C was deposited using a PDS 2010 LabCoter 2 Deposition system. A 15 μm layer of stabilized a-Se was deposited in a dedicated Se thermal evaporator, as described in [30]. Another layer of parylene-C was deposited in the same way to generate a 750 nm hole-blocking layer. Finally, a 100 × 100 mm transparent conducting layer [indium-tin oxide (ITO)] was sputtered and deposited as four 51 × 51 mm squares with ~1 mm overlap to serve as the top contact, extending beyond the active area to allow for bonding and space to pair with the scintillator.

The detector was then connected to a Varex readout system, and a scintillator was coupled to the active area of the photodiode. Three scintillators were used for various measurements, in order to best determine the performance of the photodetector itself: LANEX Fine and DRZ+ gadolynium oxysulfide (GOS) with peak emission at 510 nm, and a CsI:Tl scintillator with peak emission at 550 nm.

B. Device Characterization

The imager was characterized using an RQA5 beam quality X-ray source at Varex facilities. Lag was calculated as the percentage of counts remaining in each frame relative to the last exposed frame. Internal software (Viva) was used to calculate noise power spectrum (NPS), DQE, and MTF from the collected signal. Sensitivity was calculated as the counts/μm Gy (with a dose/frame of 11.4 μGy) as a function of applied bias, using a standard Varex a-Si FPD as a reference.

C. Modeling

The resolution performance of the FPD was simulated using a cascaded linear system model (CLSM) which models the performance of the X-ray imager as a series of independent physical processes, such as signal attenuation, gain, and optical blurring [34], [35]. The overall MTF of an X-ray imaging system is affected by various physical parameters such as k-fluorescence reabsorption, the charge carrier trapping in the blocking layer, and optical spreading in the scintillation layer [36], [37]. In this work, the equations that were used to model the series of imaging stages of the FPD, related to the properties of a-Se and GOS, were developed by previously published works [37], [38], [39], [40], [41]. To evaluate the effect of phosphor thickness on the signal blur and collection efficiency, the LANEX Fine GOS scintillator properties were considered in the MTF model and to validate the detector performance [36], [42], [43]. By comparing simulated results to experimental measurements of the MTF, we obtained a qualitative understanding of the signal blur due to the GOS scintillator layer.

III. Results and Discussion

Images at each step of fabrication of the photodetector can be seen in Fig. 2. After the second parylene deposition, visible defects appeared under the parylene layer; further discussion of their effects can be found later below. Deposition of the ITO resulted in darker areas where the ITO overlapped, which was done to provide continuous bias across the entire device. Additionally, limitations in the sputtering system generated thicker rings in some areas of each square.

The DRZ+ and the LANEX Fine scintillators were sized to accurately pair to the Varex panel active area. However, each had drawbacks: the DRZ+ was the thicker of the two, giving higher sensitivity, but greater optical blur. The LANEX Fine was thinner, giving higher resolution but lower sensitivity.

The detector was first paired to the DRZ+, and the bias voltage was ramped up to 300 V—approximately 270 V (18 V/μm) across the a-Se layer and 30 V across the parylene layers—for signal and lag measurements, which can be found in Fig. 3(a). The lag dropped to less than 1% after 4 frames (200 ms) and to 0.1% after 20 frames (1 s). While this is too long for CT scans, most single-shot images only require exposure after a waiting period, making this acceptable for our intended applications. The overall signal count [inset of Fig. 3(a)] reached just under 6000 counts with a fast rise and fall.

The scintillator was then swapped to the LANEX Fine for NPS and DQE measurements, found in Fig. 3(b). The detector showed good NPS at 300 V bias and 35 uGy/frame, under 700 counts^2 mm^2 at 6 lp/mm. The DQE is rather low across all cycles/mm, however, is in line with what can be expected at 300 V for a thin GOS layer, in which conversion efficiencies for a-Se are limited to less than 10% by the wavelength and applied field [21], [44].

Unfortunately, 300 V pushed the maximum bias the TFT could accommodate during hole collection and became unstable after performing several measurements. The defects that appeared during fabrication began to create points of failure in the pixels, and eventually resulted in bright lines of signal across the image. The bias was then reduced to 150 V (~9 V/μm) for the remaining measurements. This limits the performance of the a-Se in DQE, as high visible photon conversion is expected at fields greater than 30 V/μm, and indicates that a thinner layer of photoconductor material is required to achieve these high fields, and those required for impact ionization, and high DQE.

To understand the limitations of the detector, MTF was modeled for the TFT panel, a direct 15 μm a-Se/TFT panel, the LANEX Fine scintillator, and the entire architecture used. The results of this can be seen in Fig. 4(a). A direct a-Se detector shows only slightly reduced performance at higher line pairs compared to what the TFT is capable of resolving. Introducing the LANEX Fine scintillator significantly reduces the performance, causing an immediate drop in MTF with increasing cycles/mm due to the optical spread created from the X-ray scintillation. While GOS scintillators have a high sensitivity to X-rays, the fabrication techniques limit how well the emitted light is guided to the photodetector and are known to have lower resolution. The addition of a-Se only slightly lowers the MTF at longer cycles/mm, as it does in the case of direct detection.

Fig. 4(b) shows the measured MTF of the detector when biased at 150 V, with a fit to the data to guide the eye. Comparing this to the model of the full detector, we see that the device performance is in line with what we expect, except at lower cycles/mm; this indicated that the resolution was limited by the scintillator, and utilizing a higher resolution scintillator could lead to improved MTF. At low cycles/mm, we observe a sharp drop from unity. To investigate further, we remove the scintillator from the photodetector, perform an MTF measurement, and see the same behavior at low cycles/mm. This gives confidence that the scintillator is not the cause of the drop. In addition, the thin layer and limited charge spreading a-Se undergo [41] supports that the detector is not the cause of the drop, and rather is due to backscattering off the material behind the sensor. An image of a resolution phantom, seen in Fig. 4(c), demonstrated the performance of the detector, highlighting that six line pairs/mm can be resolved by eye.

Additional images were taken of a hand phantom and a printed circuit board, seen in Fig. 5. The appearance of image defects is highlighted by red-dashed lines. These defects degrade the resolution and performance of the detector and lead to breakdowns at higher bias, as noted above. Future detectors will add additional steps and cleaning to limit the inclusion of fabrication defects; however, it can be expected that some may appear when working with large areas and in a shared research facility.

Finally, the sensitivity of the detector was measured using the DRZ+ and a CsI:Tl scintillator, along with the detector without scintillator, shown in Fig. 6. The CsI:Tl scintillator has a peak emission at 550 nm, outside of the optimal absorption of a-Se, though it has greater inherent resolution and higher photon yields than GOS scintillators. As expected, the detector has lower sensitivity when coupled to the CsI:Tl and without a scintillator as compared to the DRZ+; the performance was, however, still good given the reduced absorption of a-Se for the CsI:Tl scintillator emission and low thickness of a-Se for direct detection. This shows good promise for both an alloyed indirect detector with a lower bandgap—tuned for absorption at 550 nm—and a thicker a-Se direct detector.

IV. Conclusion

In summary, we have fabricated and characterized an indirect, a-Se FPD with 83 μm pixel pitch and 85 × 85 mm continuous active area, demonstrating lag, NPS, DQE, and MTF acceptable for single image applications. The detector maintains an MTF greater than 0.2

at 6 cycles/mm, reaching the maximum performance of the scintillator coupled to it. The selected architecture of parylene-C planarization and hole-blocking layers give performance parameters on par with that expected from a-Se and the GOS scintillators at the biases used in this work. This provides a promising starting point for optimizing the detector; future work will explore thinner a-Se layers alloyed with Te to allow the application of higher fields (for higher DQE and impact ionization) while lowering the bandgap for utilization with longer wavelength scintillators.

Acknowledgments

This work was supported in part by the U.S. Department of Energy, Office of Science, Office of High Energy Physics under Award DE-SC0022343 and in part by the National Institutes of Health under Award 1R01EB033466.

References

[1]. Taguchi K and Iwanczyk JS, "Vision 20/20: Single photon counting X-ray detectors in medical imaging," Med. Phys., vol. 40, no. 10, Oct. 2013, Art. no. 100901.

[2]. Han JC et al. , "Single-shot dual-energy X-ray imaging with a flat-panel sandwich detector for preclinical imaging," Current Appl. Phys, vol. 14, no. 12, pp. 1734–1742, Dec. 2014.

[3]. Tsai H et al. , "A sensitive and robust thin-film X-ray detector using 2D layered perovskite diodes," Sci. Adv, vol. 6, no. 15, Apr. 2020, Art. no. eaay0815.

[4]. Ghammraoui B, Makeev A, and Glick SJ, "High-rate X-ray spectroscopy in mammography with photon counting detectors using a limited number of energy bins," Radiat. Meas., vol. 138, Nov. 2020, Art. no. 106444.

[5]. Scott CC et al. , "High-energy micrometre-scale pixel direct conversion X-ray detector," J. Synchrotron Radiat, vol. 28, no. 4, pp. 1081–1089, Jul. 2021. [PubMed: 34212871]

[6]. Ou X et al. , "Recent development in X-ray imaging technology: Future and challenges," Research, vol. 2021, Jan. 2021, Art. no. 9892152.

[7]. Zhou Y, Chen J, Bakr OM, and Mohammed OF, "Metal halide perovskites for X-ray imaging scintillators and detectors," ACS Energy Lett, vol. 6, no. 2, pp. 739–768, Feb. 2021.

[8]. Pacella D, "Energy-resolved X-ray detectors: The future of diagnostic imaging," Rep. Med. Imag, vol. 8, pp. 1–13, Jan. 2015.

[9]. Lell MM and Kachelrieß M, "Recent and upcoming technological developments in computed tomography: High speed, low dose, deep learning, multienergy," Investigative Radiol, vol. 55, no. 1, pp. 8–19, Jan. 2020.

[10]. Danielsson M, Persson M, and Sjölin M, "Photon-counting X-ray detectors for CT," Phys. Med. Biol, vol. 66, no. 3, Jan. 2021, Art. no. 03TR01.

[11]. Scholz J et al. , "Biomedical X-ray imaging with a GaAs photon-counting detector: A comparative study," APL Photon., vol. 5, no. 10, Oct. 2020, Art. no. 106108.

[12]. Ren L, Zheng B, and Liu H, "Tutorial on X-ray photon counting detector characterization," J. X-Ray Sci. Technol, vol. 26, no. 1, pp. 1–28, Feb. 2018.

[13]. Kim J, Park S, Hegazy M, and Lee S, "Comparison of a photon-counting-detector and a CMOS flat-panel-detector for a micro-CT," in Proc. IEEE Nucl. Sci. Symp. Med. Imag. Conf. (NSS/MIC), Oct. 2013, pp. 1–4.

[14]. McCollough CH, Leng S, Yu L, and Fletcher JG, "Dual- and multi-energy CT: Principles, technical approaches, and clinical applications," Radiology, vol. 276, no. 3, pp. 637–653, Sep. 2015. [PubMed: 26302388]

[15]. Vock P and Szucs-Farkas Z, "Dual energy subtraction: Principles and clinical applications," Eur. J. Radiol, vol. 72, no. 2, pp. 231–237, Nov. 2009. [PubMed: 19423259]

[16]. Szucs-Farkas Z, Patak MA, Yuksel-Hatz S, Ruder T, and Vock P, "Single-exposure dual-energy subtraction chest radiography: Detection of pulmonary nodules and masses in clinical practice," Eur. Radiol, vol. 18, no. 1, pp. 24–31, Jan. 2008. [PubMed: 17899105]

[17]. Maurino SL, Ghanbarzadeh S, Ghaffari S, and Karim KS, “Novel multi-energy X-ray detector allows for simultaneous single-shot acquisition of digital radiography and tissue-subtracted images,” in Proc. ECR EPOS Eur. Congr. Radiol. (ECR), Jan. 2019. Accessed: Aug. 10, 2022. [Online]. Available: https://epos.myesr.org/poster/esr/ecr2019/C-3350

[18]. Shi L et al. , “Characterization and potential applications of a dual-layer flat-panel detector,” Med. Phys, vol. 47, no. 8, pp. 3332–3343, Aug. 2020. [PubMed: 32347561]

[19]. Wang W et al. , “High-resolution model-based material decomposition in dual-layer flat-panel CBCT,” Med. Phys, vol. 48, no. 10, pp. 6375–6387, Oct. 2021. [PubMed: 34272890]

[20]. Swaby A, Abbaszadeh S, Wang AS, and Willemink MJ, “Dual-layer flat panel detector with a-Se top layer for opportunistic screening of coronary artery calcium: A simulation study,” Proc. SPIE, vol. 12031, Apr. 2022, Art. no. 1203143.

[21]. Hellier K, Mollov I, Pryor P, and Abbaszadeh S, “A dual-layer direct/indirect flat panel detector for improved material decomposition: First studies of the indirect layer,” Proc. SPIE, vol. 12463, pp. 520–524, Apr. 2023.

[22]. Zhao W and Rowlands JA, “X-ray imaging using amorphous selenium: Feasibility of a flat panel self-scanned detector for digital radiology,” Med. Phys, vol. 22, no. 10, pp. 1595–1604, Oct. 1995. [PubMed: 8551983]

[23]. Hajdok G, Battista JJ, and Cunningham IA, “Fundamental X-ray interaction limits in diagnostic imaging detectors: Spatial resolution,” Med. Phys, vol. 35, no. 7, pp. 3180–3193, Jun. 2008. [PubMed: 18697543]

[24]. Zhu M, Niu G, and Tang J, “Elemental Se: Fundamentals and its optoelectronic applications,” J. Mater. Chem. C, vol. 7, no. 8, pp. 2199–2206, Feb. 2019.

[25]. Huang H and Abbaszadeh S, “Recent developments of amorphous selenium-based X-ray detectors: A review,” IEEE Sensors J, vol. 20, no. 4, pp. 1694–1704, Feb. 2020.

[26]. Allec N and Karim KS, “A balanced filterless K-edge energy window multilayer detector for dual energy computed tomography,” Proc. SPIE, vol. 7622, pp. 1420–1429, Mar. 2010.

[27]. Kasap S et al. , “Amorphous and polycrystalline photoconductors for direct conversion flat panel X-ray image sensors,” Sensors, vol. 11, no. 5, pp. 5112–5157, May 2011. [PubMed: 22163893]

[28]. Tanioka K et al. , “An avalanche-mode amorphous selenium photoconductive layer for use as a camera tube target,” IEEE Electron Device Lett, vol. EDL-8, no. 9, pp. 392–394, Sep. 1987.

[29]. Scheuermann JR, Howansky A, Hansroul M, Léveillé S, Tanioka K, and Zhao W, “Toward scintillator high-gain avalanche rushing photoconductor active matrix flat panel imager (SHARP-AMFPI): Initial fabrication and characterization,” Med. Phys., vol. 45, no. 2, pp. 794–802, Feb. 2018. [PubMed: 29171067]

[30]. Hellier K, Stewart DA, Read J, Sfadia R, and Abbaszadeh S, “Tuning amorphous selenium composition with tellurium to improve quantum efficiency at long wavelengths and high applied fields,” ACS Appl. Electron. Mater, vol. 5, no. 5, pp. 2678–2685, May 2023. [PubMed: 37250467]

[31]. Park W-D and Tanioka K, “Spectral responses of Te-doped a-Se high-gain avalanche rushing amorphous photoconductor (HARP) films for a solid state image sensor,” Jpn. J. Appl. Phys, vol. 42, no. 4B, pp. 1954–1956, Apr. 2003.

[32]. Reznik A et al. , “Avalanche multiplication phenomenon in amorphous semiconductors: Amorphous selenium versus hydrogenated amorphous silicon,” J. Appl. Phys, vol. 102, no. 5, Sep. 2007, Art. no. 053711.

[33]. Kannan H et al. , “Ultralow dark currents in avalanche amorphous selenium photodetectors using solution-processed quantum dot blocking layer,” ACS Photon, vol. 7, no. 6, pp. 1367–1374, Jun. 2020.

[34]. Cunningham IA, “Applied linear-system theory,” in Handbook of Medical Imaging, vol. 1. Bellingham, WA, USA: SPIE, 2000, pp. 79–222.

[35]. Panneerselvam DM and Kabir MZ, “Evaluation of organic perovskite photoconductors for direct conversion X-ray imaging detectors,” J. Mater. Sci., Mater. Electron, vol. 28, no. 10, pp. 7083–7090, May 2017.

[36]. Badano A, "Optical blur and collection efficiency in columnar phosphors for X-ray imaging," Nucl. Instrum. Methods Phys. Res. A, Accel. Spectrom. Detect. Assoc. Equip, vol. 508, no. 3, pp. 467–479, Aug. 2003.

[37]. Zhao W, Ristic G, and Rowlands JA, "X-ray imaging performance of structured cesium iodide scintillators," Med. Phys, vol. 31, no. 9, pp. 2594–2605, Sep. 2004. [PubMed: 15487742]

[38]. Hubbell J and Seltzer S, "Tables of X-ray mass attenuation coefficients and mass energy-absorption coefficients 1 keV to 20 MeV for elements Z = 1 to 92 and 48 additional substances of dosimetric interest," Nat. Inst. Standards Technol. (NIST), Gaithersburg, MD, USA, 1995. Accessed: Feb. 5, 2023. [Online]. Available: http://physics.nist.gov/PhysRefData/XrayMassCoef/cover.html and

[39]. Siewerdsen JH, Antonuk LE, El-Mohri Y, Yorkston J, Huang W, and Cunningham IA, "Signal, noise power spectrum, and detective quantum efficiency of indirect-detection flat-panel imagers for diagnostic radiology," Med. Phys, vol. 25, no. 5, pp. 614–628, May 1998. [PubMed: 9608470]

[40]. Kabir MZ, Rahman MW, and Shen WY, "Modelling of detective quantum efficiency of direct conversion X-ray imaging detectors incorporating charge carrier trapping and K-fluorescence," IET Circuits, Devices Syst., vol. 5, no. 3, p. 222, 2011.

[41]. Kabir MZ, "Effects of charge carrier trapping on image resolution of multilayer photoconductive detectors: Application to amorphous selenium X-ray detectors," Radiation, vol. 2, no. 1, pp. 91–99, Jan. 2022.

[42]. Rahn JT et al. , "High resolution X-ray imaging using amorphous silicon flat-panel arrays," IEEE Trans. Nucl. Sci, vol. 46, no. 3, pp. 457–461, Jun. 1999.

[43]. Cho MK et al. , "Measurements of X-ray imaging performance of granular phosphors with direct-coupled CMOS sensors," IEEE Trans. Nucl. Sci, vol. 55, no. 3, pp. 1338–1343, Jun. 2008.

[44]. Pai DM and Enck RC, "Onsager mechanism of photogeneration in amorphous selenium," Phys. Rev. B, Condens. Matter, vol. 11, no. 12, pp. 5163–5174, Jun. 1975.

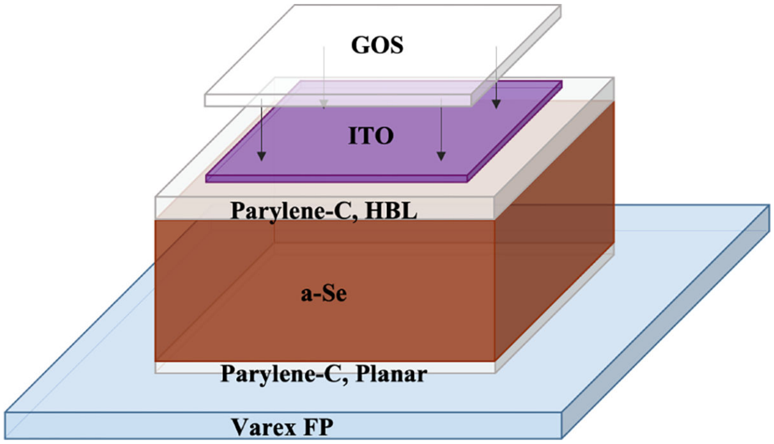

Fig. 1.

Architecture of the a-Se flat panel imager, with 1) an 83 μm pitch, 1024 × 1024 TFT backplane, 2) 100 nm parylene-C planarization layer, 3) 15 μm stabilized a-Se, 4) 750 nm parylene-C blocking layer, and 5) a 75 nm ITO transparent top contact, paired with a DRZ+ or LANEX Fine GOS scintillator (not to scale).

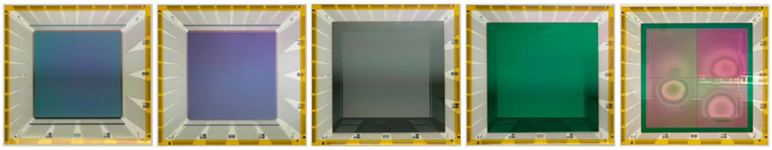

Fig. 2.

Images of the a-Se photodiode FPD at each step of fabrication, from left to right: 1) Uncoated TFT panel, 2) parylene planarization layer, 3) 15 um a-Se, 4) parylene HBL, 5) ITO (deposited in four 2” squares). Pictures of the detector coupled to a scintillator are not shown.

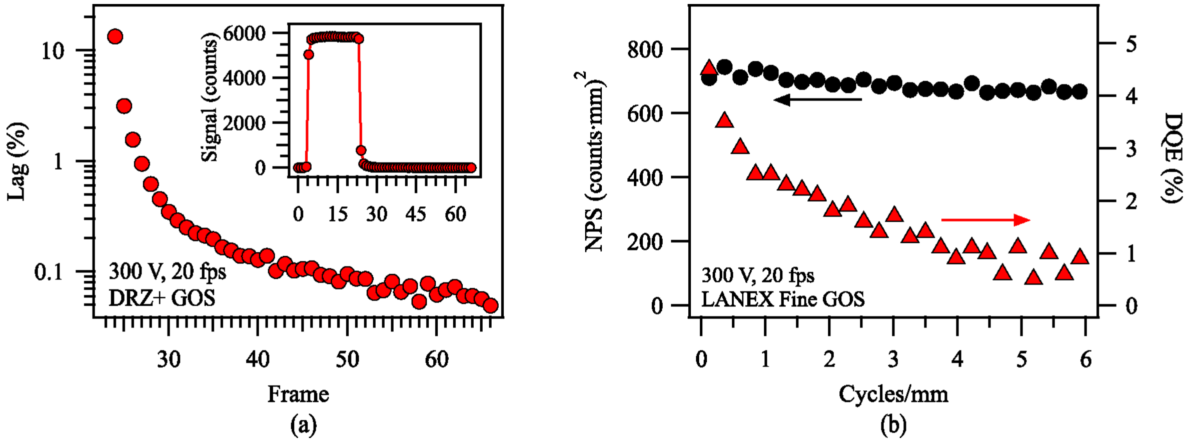

Fig. 3.

(a) Calculated lag of detector, based on the signal (inset) taken with the DRZ+ scintillator. (b) NPS (left axis, black circles) and DQE (right axis, red triangles) of the detector with the LANEX Fine scintillator.

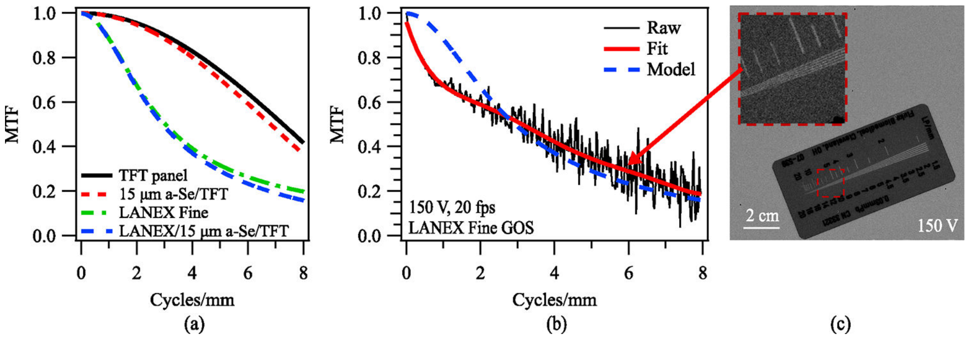

Fig. 4.

(a) Simulated MTF for the 83 um pixel pitch TFT panel used in this work, 15 um a-Se on the panel, a LANEX Fine scintillator, and the combination of the LANEX Fine scintillator above 15 um a-Se on the TFT panel. (b) Modulated transfer function (MTF) of imager using slant edge technique compared with the model for this detector. (c) Image of a resolution phantom demonstrating resolution at 6 line pairs per millimeter.

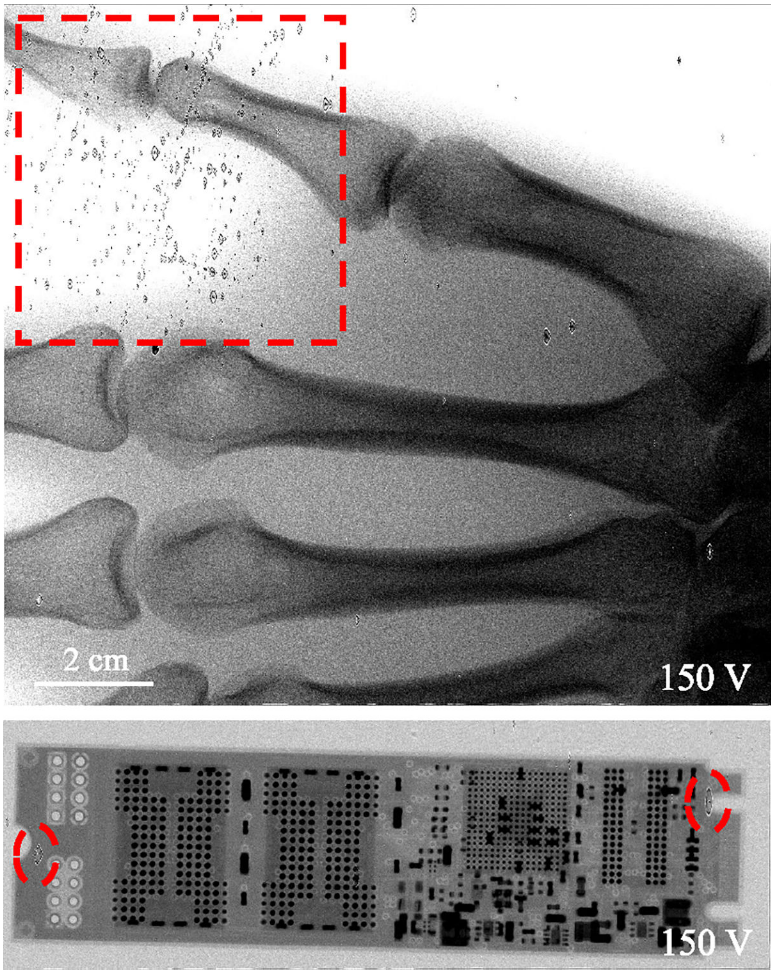

Fig. 5.

(Bottom) PCB board and (top) hand phantom with several defects highlighted in red.

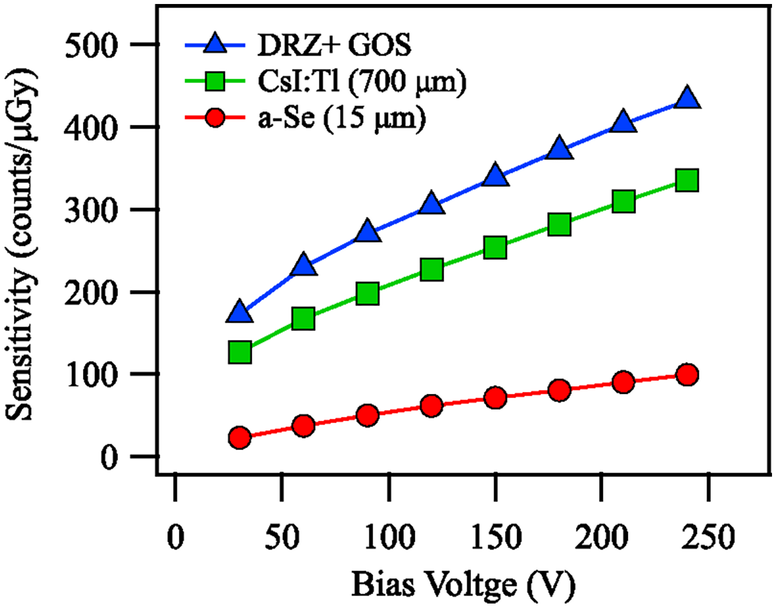

Fig. 6.

Sensitivity of the detector (dose/frame of 11.4 μGy) when paired with a DRZ+ GOS scintillator (blue triangles), a CsI:Tl scintillator (green squares), and without a scintillator (red circles).